Combining x-ray real and reciprocal space mapping techniques to explore the epitaxial growth of semiconductors

S Magalhães[1,*] , **J S Cabaço[2], O Concepción[3]** , **D Buca[3], M Stachowicz[4], F Oliveira[5], M F Cerqueira[5,6], K Lorenz[1,7] and E Alves[1]**

[1] IPFN, Instituto de Plasmas e Fusão Nuclear, Campus Tecnológico e Nuclear, Instituto Superior Técnico, Universidade de Lisboa, Estrada Nacional 10, 2695-066 Bobadela LRS, Portugal

[2] Institute of Ion Beam Physics and Materials Research, Helmholtz-Zentrum Dresden-Rossendorf, 01328 Dresden, Germany

[3] Peter Gruenberg Institute 9 (PGI-9), Forschungszentrum Juelich, 52425 Juelich, Germany

[4] Institute of Physics, Polish Academy of Sciences, Al. Lotników 32/46, PL-02-668 Warsaw, Poland

[5] Centro de Física, Universidade do Minho, Campus de Gualtar, 4710-057 Braga, Portugal

[6] International Iberian Nanotechnology Laboratory, Braga, Portugal

[7] Instituto de Engenharia de Sistemas de Computadores-Microsystems and Nanotechnology (INESC-MN), Lisboa, Portugal

E-mail: smagalhaes@ctn.tecnico.ulisboa.pt

CrossMark

Abstract

In the present work, the importance of determining the strain states of semiconductor compounds with high accuracy is demonstrated. For the matter in question, new software titled *LAPAs*, the acronym for LAttice PArameters is presented. The lattice parameters as well as the chemical composition of $Al_{1-x}In_xN$ and $Ge_{1-x}Sn_x$ compounds grown on top of GaN- and Ge-buffered c-Al_2O_3 and (001) oriented Si substrates, respectively, are calculated via the real space Bond's method. The uncertainties in the lattice parameters and composition are derived, compared and discussed with the ones found via x-ray diffraction reciprocal space mapping. Broad peaks lead to increased centroid uncertainty and are found to constitute up to 99% of the total uncertainty in the lattice parameters. Refraction correction is included in the calculations and found to have an impact of 0.001 Å in the lattice parameters of both hexagonal and cubic crystallographic systems and below 0.01% in the quantification of the InN and Sn contents. Although the relaxation degrees of the nitride and tin compounds agree perfectly between the real and reciprocal-spaces methods, the uncertainty in the latter is found to be ten times higher. The impact of the findings may be substantial for the development of applications and devices as the intervals found for the lattice match the condition of $Al_{1-x}In_xN$ grown on GaN templates vary between ~1.8% (0.1675–0.1859) and 0.04% (0.1708–0.1712) if derived via the real- and reciprocal spaces methods.

---

* Author to whom any correspondence should be addressed.

1. Introduction

Combining real space ω-scans with reciprocal space mapping x-ray diffraction (XRD) techniques may overcome partially the different limitations associated with both methodologies for determining the lattice parameters of thin films. As a matter of fact, ω-scans are frequently accumulated with an open-detector set-up while reciprocal space maps are often measured with add-on optics in both primary and secondary beam paths [1–5]. The measured Bragg peak is expected to be broader in the former resulting in a higher probability of partial peak overlapping between the scattering events due to the thin film and the ones of the supporting crystal. Partial peak overlapping increases the diffraction centroid uncertainty, resulting in an increased uncertainty in the lattice parameters. In the case of the latter, reciprocal space maps are highly time-consuming due to the wide ranges of probing through combinations of ω- and 2θ- angles with convenient statistics. The lower statistics expected in the case of the reciprocal space mapping introduce uncertainties in the diffraction spot centroid. The crystalline mosaicity becomes accessible from the peak-shape and the broadening of the fits of a reciprocal space map (RSM) along specific ω- and $2\theta-\omega$ directions [4]. In particular, the tilt angle and the lateral coherence length may be determined from a ω-scan while the vertical coherence length and the heterogeneous strain are causes of the broadening and change of the peak-shape of a $2\theta-\omega$ scan. Therefore, higher uncertainties in the full width at half maximum (FWHM) and in the peak-shape anticipate higher uncertainties associated with the quantification of crystallographic defects. Indeed, the density of dislocations depends on a specific Burgers vector determined by its direction and magnitude (lattice parameters) [4, 6–8].

Higher lattice parameter uncertainties also predict higher chemical composition uncertainties as the latter are often derived using Vegard's rule [9] together with the Poisson law [10, 11]. Moreover, the uncertainties in the lattice parameters and the composition of semiconductor compounds propagate to the determination of its strain states [5, 12, 13]. As an example, according to Vegard's rule, [9] $Al_{1-x}In_xN$ thin films grown on GaN templates are under tensile strain for InN molar fractions below $\sim$17.2%, while above it, the ternary compound is subjected to compressive strain. The $\sim$17.2% InN content, or the so-called '*magic*' lattice match condition, is the condition for strain-free growth of $Al_{1-x}In_xN$ on GaN virtual substrates [5, 14]. On the one hand, the quantification of the uncertainties in the lattice parameters measured by XRD may affect the interpretation of several compound's chemical composition and its derived strain state. On the other hand, the inaccuracy in the determination of the lattice match

condition between the $Al_{1-x}In_xN$ and the GaN may reduce the quality of promising applications such as Bragg mirrors or microcavities [14, 15], high electron mobility transistors [16, 17] and applications regarding a sacrificial layer for the development of 3D GaN crystalline structures through chemical etching [14, 18]. An important impact of the uncertainties in the mentioned physical quantities on related technologies is, thus, expected. In fact, the increased uncertainty in the strain states additionally propagates to the quantification of the strain-induced defects affecting the conclusions related to the large band offsets and the strong polarization fields' typical in the nitride compounds.

Another important layered system where the effects of strain govern the optoelectronic fundamental properties is the $Ge_{1-x}Sn_x$ grown on Ge buffer layers and Si substrates [19–22]. Actually, if the $Ge_{1-x}Sn_x$ layer is relaxed, calculations based on the density functional theory propose a direct band-gap for the binary which would enhance the already tremendous potential of the tin compounds [23]. The uncertainties in the lattice parameters, thus, in the composition of the $Ge_{1-x}Sn_x$ binary are expected to affect the interpretation of the solubility of Sn in Ge which is limited. Phase separation and segregation tend to decrease the solubility for higher Sn content $Ge_{1-x}Sn_x$ pure random compounds reducing the crystalline quality with increasing tin content [24, 25]. Therefore, higher uncertainties in the crystalline quality are expected. Specifically, uncertainties in the relaxation of the lattice strain induce higher uncertainties in the tilt of the crystallites and in the density of dislocations as it will generate higher uncertainties in the pseudomorphism degree even for low Sn content $Ge_{1-x}Sn_x$ [25].

As controlled lattice parameters are fundamental for optoelectronic and microelectronic devices operating in the near-infrared region, higher uncertainties may limit the development of Si-compatible direct band-gap materials. Accordingly, the quantification of the lattice parameters and chemical composition uncertainties of the groups III-nitrides and IV compounds may strongly affect the interpretation of the strain states imposed to the surface layer, i.e. the relevant and technologically driven crystal. The quantification of the uncertainties in the lattice parameters and chemical composition may also be relevant for II–VI semiconductors where HgCdTe and CdTe are important examples. In fact, the ternary is a promising candidate for high-performance infrared detectors and imaging focal plane arrays [26]. Furthermore, HgCdTe is lattice matched to CdZnTe at a Cd molar fraction of 0.96. Thus, if grown coherently it may increase dramatically the performance of HgCdTe devices. In fact, Pan *et al* demonstrated the pseudomorphic growth of sets of CdZnTe/CdTe superlattices, the so-called dislocation filtering layers, stacked in-between

CdTe layers, capped and buffered by a thicker CdTe layer grown on a GaAs (211) B substrate [27, 28]. The CdTe layers outside the superlattice become compressively strained which facilitates in-plane lattice matching with HgCdTe. Moreover, the growth of the dislocation filtering layers adjuvants the reduction of dislocation densities, thus improving the crystalline quality of the CdTe layers [29]. Detailed analysis of the XRD rocking curves of CdZnTe/CdTe superlattices may be found in [28] while the analysis of the reciprocal space mapping of HgCdTe grown on alternative substrates may be found in [30].

In the current work, the nominal crystal structures of a set of $Al_{1-x}In_xN$ and two sets of $Ge_{1-x}Sn_x$ compound epilayers grown by metal organic chemical vapour deposition (MOCVD), molecular beam epitaxy (MBE) and chemical vapour deposition (CVD), respectively, are described in section 2. Section 2 also contains a description of the experimental technique used to characterize the samples (XRD). The procedure to determine the uncertainties in the lattice parameters and the chemical composition is addressed in supplemental information S1. To the best knowledge of the authors, it is the first time that a detailed comparison between the main sources of uncertainties in the determination of the lattice parameters, chemical composition, and strain derived via the real- and reciprocal space approaches is presented. In section 3, the composition and strain dependence upon the InN/Sn contents are characterized by the x-ray reciprocal space mapping and ω-scans. The Bond's method, a high accuracy real-space method for determining the lattice parameters through the reduction of experimental and instrumental errors, is used [31]. It consists in measuring glancing incidence/exit ω-scans of asymmetric and symmetric reflections. One of the advantages of Bond's method is to reduce important systematic experimental errors. In particular, the position of the sample with respect to the sample holder may affect the measured 2θ, thus, affecting the measured lattice parameter. Other effects contributing to a mis-interpretation of the measured lattice parameters are the presence of point defects as described in [32], the presence of misfit dislocations in partially relaxed layers, [33] and the inhomogeneous tilt of the crystal's lattice [34, 35]. The effects of the above defects on the lattice parameters are not addressed in this work. Moreover, the accuracy in the determination of the lattice parameters may be increased by measuring more than 1 asymmetric reflection as in the case of Bond's method. In fact, by employing the Fewster and Andrew method, [34] the accuracy may increase up to one order of magnitude (0.000 01 Å) as demonstrated in [36] for the case of GaN films grown on AlN/6H SiC (0001) substrates. A detailed description of Bond's method is addressed in S1. The main conclusions of the manuscript are conveyed in section 4.

2. Samples and experimental techniques description

In order to deepen the knowledge about the hetero-epitaxial crystal growth, two sets of samples with different Bravais lattices (hexagonal $Al_{1-x}In_xN$ and cubic $Ge_{1-x}Sn_x$) are studied. The first set, designated as the S series, is composed of aluminium indium nitride ($Al_{1-x}In_xN$) thin films grown by MOCVD with increasing InN contents grown on top of an ~1000 nm thick gallium nitride (GaN) buffer layer and wurtzite c-sapphire substrate. In one sample, S1, the ternary compound was grown on top of GaN-free standing substrate [37]. The ternary film thicknesses are about 100 nm and the chemical compositions were accurately derived through Rutherford backscattering spectrometry using the high accuracy method described in [38] The relaxation degree measured with respect to the GaN- templates (or substrate) is calculated. The proposed methodology is also applied to ~200 nm thick germanium tin layers ($Ge_{1-x}Sn_x$) with increasing tin contents grown on top of an ~100 nm germanium template and commercial (100) oriented silicon substrate. The $Ge_{1-x}Sn_x$ compound films (C series) were grown by MBE. Complementarily, the relaxation degrees of three $Ge_{1-x}Sn_x$ films (A series) with different nominal thicknesses (190 nm (A1), 290 nm (A2) and 100 nm (A3)) and Sn contents (8.5% (A1), 9% (A2) and 12% (A3)) grown by CVD is studied. Detailed descriptions of the growth of the nitride compounds can be found in [39] while the growth of the tin compounds by MBE and CVD are communicated in [40–42], respectively. In both latter cases, the Ge template imposes compressive strain to the surface tin layer forcing it to adopt pseudomorphic behaviour. All the samples were measured in a Bruker D8 AXS diffractometer using a Göbel parabolic mirror, followed by a 0.2 mm wide slit to limit the horizontal divergence and a Ge 220 monochromator to collimate the x-ray beam and to mitigate the $K\alpha_2$ radiation. According to [43], the application of a monochromator may be sufficient to eliminate the off-plane divergence which may affect the angular positions of the diffraction maxima while the horizontal divergence is below 0.005°. The diffracted x-rays were collected using a point focus detector with an active area of 4×15 mm^2 located at 35 cm distance from the sample along the secondary diffractometer beam path. For the reciprocal space mapping and the radial 2θ–ω scans, a 0.1 mm wide slit was included in front of the detector to further reduce the horizontal beam divergence. The ω-scans were collected without the 0.1 mm wide slit. According to the employed optics, the resulting sample's probing area is ~0.2×1 cm^2 for the normal incidence of the x-rays. The broadenings of the diffraction peaks caused by the instrumental resolution acquired on the Si wafer provided by the diffractometer manufacturer were found to be at least 100 times lower than the broadenings of the measured 2θ–ω and ω-scans (not shown). Furthermore, very low levels of asymmetry were deduced from the diffracted curves suggesting a negligible effect of the instrumental function in the accuracy and precision in the determination of the lattice parameters of the studied crystals. The alignment procedure is exhaustively described in S2. *LAPAs*, an acronym for '*LAttice PArameters*' software is made available in its final version to the research community on the www.MROX.eu website while previous versions were employed in several studies [1, 5, 44–50]. The software was used to estimate the lattice parameters, chemical composition of the compounds, output Pseudo-Voigt (PV) coefficients, FWHM, scan asymmetry, and

respective uncertainties, as well as generic *.dat output files for representation in graphical software are provided in around two minutes. Detailed description of the *LAPAs* software is addressed in S3.

3. Experimental results

The lattice parameters of the relaxed GaN, AlN, InN, Si, Ge, Sn and respective stiffness coefficients considered in the current work are listed in table 1. According to the dispersion of the values found in the literature, uncertainties of 0.001 Å and 5 GPa are used for the relaxed lattice parameters and respective stiffness coefficients. Both quantities are fundamental to derive the chemical composition uncertainties while the former are relevant to determine the uncertainty in the relaxation of the surface layer.

With respect to the Si, Ge and Sn cubic crystals, the constants indicated in table 1 correspond to the average of the published parameters determined for the last two decades as exhaustively compared and discussed in the supplemental information S1 of [1]

3.1. Aluminium indium nitride thin films grown on GaN templates (hexagonal)

In order to compare the relaxation of the $Al_{1-x}In_xN$ thin films derived by reciprocal space mapping and real-space via Bond's method [31], the lattice parameters and composition of the ternary compound and the lattice parameters of the respective templates are calculated. Figure 1 shows the $10\bar{1}5$ RSMs around the GaN and $Al_{1-x}In_xN$ diffraction spots of the S1, S2, S3 and S4 samples. Simulations using 2D-Gaussians of the respective experimental RSMs are included on the right side of each individual measurement shown in figure 1. Simulations (and fittings) were executed using the *RSM* software described in [1] Cu Kα_2 residuals observed in all the measured RSMs are accounted for in the simulations through an additional 2D-Gaussian function. Generically, the asymmetric $10\bar{1}5$ reciprocal lattice point is fitted using 2D-Gaussians. Then, the solution is refined through the PV's function for the cuts along orthogonal directions calculated for the rotation of the different diffraction spots. High agreement between the simulations and the experimental RSM is found.

From the optimized GaN and $Al_{1-x}In_xN$ centroids $(Q_{\hat{x}}, Q_{\hat{z}})$ included in table 2 and the appropriate relation for the interplanar distance of an hexagonal unit cell [56], the in-plane $(a = \frac{2\pi \sqrt{\frac{4}{3}(h^2+hk+k^2)}}{Q_{\hat{x}}})$ and out-of-plane $(c = \frac{2\pi l}{Q_{\hat{z}}})$ lattice parameters are derived. $h = 1, k = 0, l = 5$ correspond to the Miller indexes for the measured reflection. With respect to the GaN, the derived $Q_{\hat{x}}/Q_{\hat{z}}$ is higher/lower for sample S1 (grown on free-standing GaN) compared to S2 to S4 (grown on sapphire) resulting in a lower/higher calculated *a*-/*c*- lattice parameter. In fact, thick GaN templates grown on top of sapphire-*c* substrates are, typically, slightly compressive [57]. It is interesting to note the absence of any additional diffraction spots other than the ones associated to the GaN buffer layer/substrate, the

$Al_{1-x}In_xN$ ternary compound and to the remaining Kα_2 not completely mitigated by the used optics. Therefore, according to [58], a high density of misfit dislocations is not expected and the simple procedure to calculate the lattice parameters based on the $(Q_{\hat{x}}, Q_{\hat{z}})$ centroids is suggested to be accurate.

The ternaries reveal a high degree of pseudomorphism with the respective binaries, in spite of the differences between the InN contents depicted in inset figure 1. In fact, Δa_{RSM} $(\equiv a_{Al_{1-x}In_xN} - a_{GaN})$ is found to be 0.0011 Å, 0.0016 Å, -0.0001 Å and 0.0005 Å for samples S1, S2, S3 and S4, respectively. Δa_{RSM} is found to be similar to the assumed uncertainties for the relaxed lattice parameters of the binaries (0.001 Å). The calculation of the uncertainties of the bilayer *a*- and *c*-lattice parameters follows the description in [1]. Such quantities depend exclusively on $\Delta Q_{\hat{x}}$ and Δ, i.e. the uncertainties in diffraction spot centroids along Q_x and Q_z, respectively. On the other hand, $\Delta Q_{\hat{x}}$ and $\Delta Q_{\hat{z}}$ are determined through PV refinement of the optimized 2D-Gaussian solution. The PV fittings allow accounting for the peak's *wing* through the Lorentzian fraction included in a standard PV function [4]. The higher fit quality using a PV distribution rather than a Gaussian one results in lower uncertainties for the relevant quantities, in particular, to the diffraction centre.

Evidenced in figure 1, the $Al_{1-x}In_xN$ $Q_{\hat{z}}$ decreases from the left of the right side showing increasing ternary's c-lattice parameter, thus, the InN incorporation is increasing in the same direction: from the left to the right. In figure 2(a$_1$), the optimized GaN (represented with star symbols) and the $Al_{1-x}In_xN$ $(Q_{\hat{x}}, Q_{\hat{z}})$ (open squares) diffraction spots centres as well as the reciprocal space units calculated for relaxed AlN, $(Q_{x0}, Q_{z0})_{AlN} \sim (23.32, 63.08)$ nm^{-1}, and InN, $(Q_{x0}, Q_{z0})_{InN} \sim (20.51, 55.08)$ nm^{-1}, are represented. As depicted in table 1, the relaxed AlN lattice parameters are smaller than the ones for the InN crystal. Therefore, the reciprocal relation between $(Q_{\hat{x}}, Q_{\hat{z}})$ in the reciprocal-space and the lattice parameters calculated in real-space is evidenced by the lower $(Q_{\hat{x}}, Q_{\hat{z}})$ pair derived for the relaxed InN. What is more, the $(Q_{x0}, Q_{z0})_{Al1-xInxN}$ pairs calculated for the entire compositional range $(0 \leqslant x_{InN} \leqslant 1)$ are included in figure 2(a$_1$). The calculated $(Q_{x0}, Q_{z0})_{Al1-xInxN}$ constitute the reciprocal space coordinates that satisfy the condition for full relaxation. Thereby, the line connecting $(Q_{x0}, Q_{z0})_{InN}$ and $(Q_{x0}, Q_{z0})_{AlN}$ that crosses the sets of $(Q_{x0}, Q_{z0})_{Al1-xInxN}$ pairs for a given composition is defined as the full relaxation line $(R = 1)$ [59]. To obtain $(Q_{x0}, Q_{z0})_{Al1-xInxN}$, Vegard's rule is applied considering the relaxed AlN and InN parameters indicated in table 1. The ternary's stoichiometry is employed to calculate the relaxed $Al_{1-x}In_xN$ (Q_{x0}, Q_{z0}) for the 4 derived InN contents. The dash-dotted lines overlapped with the $R = 1$ line are, thus, calculated accounting the uncertainties in the composition of the compound in the *a*- and *c*-lattice parameters as $a_{0,Al_{1-x}In_xN}|_-^+ = a_{0,InN}(x_{InN} \pm \Delta x_{InN}) + a_{0,AlN}(1 - x_{InN} \pm \Delta x_{InN})$ where the '$\pm$' signs are chosen in order to maximize and minimize $a_{0,Al_{1-x}In_xN}$, respectively. After the calculation of the relaxed lattice parameters, follows the conversion to reciprocal space units and representation in figure 2(a$_1$).

J. Phys. D: Appl. Phys. **56** (2023) 245102

S Magalhães *et al*

Table 1. In- ($a_{||}$) and out-of-plane ($a_{\perp}$) relaxed lattice parameters as well as C_{13} and C_{33} stiffness coefficients corresponding to GaN, AlN and InN, Si, Ge, Sn crystals used to determine the InN and the Sn contents in the $Al_{1-x}In_xN$ and the $Ge_{1-x}Sn_x$ compounds, respectively.

Material	$a_{||}$ (Å)	$a_{\perp}$ or c (Å)	C_{13} (GPa)	C_{33} (GPa)
GaN	3.1896 [51]	5.1855 [51]	103 [52]	405 [52]
AlN	3.111 [53]	4.98 [53]	99 [54]	389 [54]
InN	3.5377 [54]	5.7037 [54]	121 [55]	182 [55]
Si [1]	5.431	5.431	63.9	165.7
Ge [1]	5.658	5.658	47.9	129.2
Sn [1]	6.49	6.49	29.3	67.6
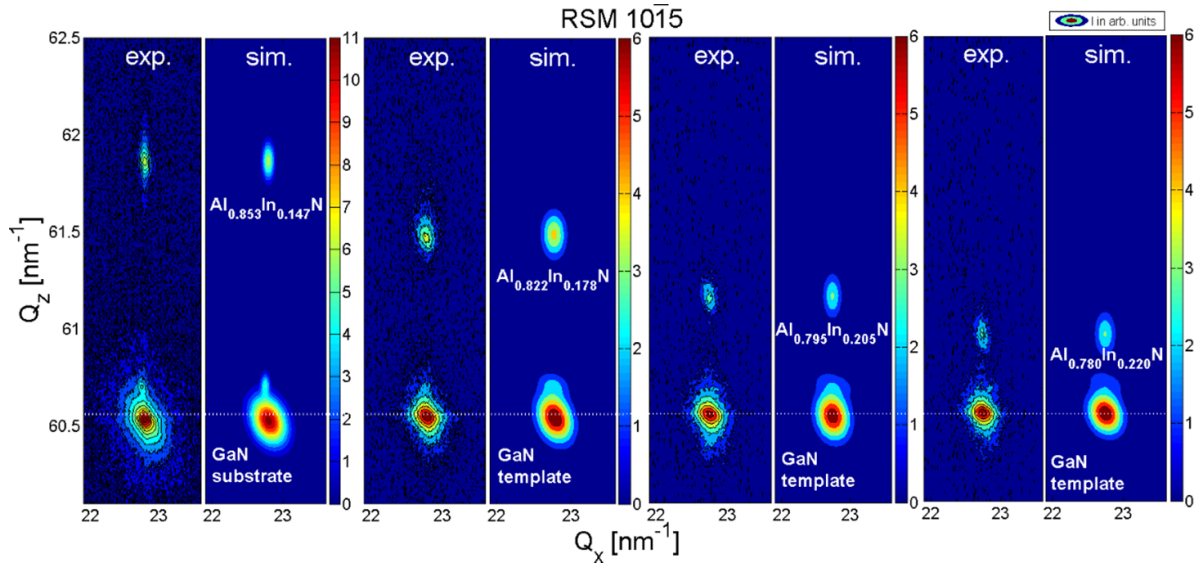
Figure 1. Experimental and simulated using 2D-Gaussians reciprocal space maps around the $10\bar{1}5$ GaN and $Al_{1-x}In_xN$ reciprocal lattice points. The $Al_{1-x}In_xN$ $Q_{\hat{z}}$ decreases from the left to the right (S1 to S4 sample) indicating higher c-lattice parameter, thus, higher InN content. The horizontal dashed-dot line highlights the slightly increasing GaN c-lattice parameter measured for sample S1.

Table 2. GaN and $Al_{1-x}In_xN$ in-plane (a-) and out-of-plane (c-) lattice parameters calculated using the optimized, $\omega_{10\bar{1}4}^{+/-}$ and $\omega_{0004}^{+/-}$ centres as well as the derived InN contents calculated from the AlN, InN relaxed lattice parameters and respective uncertainties indicated in table 1. The relevant uncertainties are included. Poisson law was used together with Vegard's rule to determine the chemical composition.

Sample		$Q_{\hat{x}}$ (nm^{-1})	$Q_{\hat{z}}$ (nm^{-1})	a (Å)	c (Å)	InN molar fraction
S1	GaN	22.7969 ± 0.0039	60.5329 ± 0.0038	3.1825 ± 0.0011	5.1899 ± 0.0007	—
	AlInN	22.7894 ± 0.0058	61.1869 ± 0.0124	3.1836 ± 0.0015	5.0778 ± 0.0021	0.1474 ± 0.0053
S2	GaN	22.7816 ± 0.0040	60.5495 ± 0.0042	3.1847 ± 0.0011	5.1885 ± 0.0007	—
	AlInN	22.7698 ± 0.0095	61.4886 ± 0.0143	3.1863 ± 0.0019	5.1092 ± 0.0024	0.1778 ± 0.0055
S3	GaN	22.7433 ± 0.0047	60.5552 ± 0.0044	3.1900 ± 0.0013	5.1880 ± 0.0007	—
	AlInN	22.7438 ± 0.0066	61.1690 ± 0.0124	3.1899 ± 0.0019	5.1359 ± 0.0021	0.2045 ± 0.0055
S4	GaN	22.7437 ± 0.0053	60.5598 ± 0.0045	3.1900 ± 0.0015	5.1876 ± 0.0008	—
	AlInN	22.7397 ± 0.0071	60.9594 ± 0.0119	3.1905 ± 0.0020	5.1536 ± 0.0021	0.2204 ± 0.0059

Sample		$\omega_{10\bar{1}4}^{+}$ (deg)	$\omega_{10\bar{1}4}^{-}$ (deg)	ω_{0004}^{+} (deg)	ω_{0004}^{-} (deg)	$a_{||}$ (Å)	c (Å)	InN molar fraction
S1	GaN	15.8624 ± 0.0001	113.8514 ± 0.0001	36.4760 ± 0.0001	143.6451 ± 0.0001	3.1826 ± 0.0001	5.1903 ± 0.0001	—
	AlInN	17.2458 ± 0.0002	113.4200 ± 0.0002	37.4111 ± 0.0002	142.7058 ± 0.0002	3.1824 ± 0.0002	5.0784 ± 0.0001	0.1469 ± 0.0002
S2	GaN	15.6587 ± 0.0001	113.6254 ± 0.0001	36.2588 ± 0.0001	143.3951 ± 0.0001	3.1842 ± 0.0001	5.1883 ± 0.0001	—
	AlInN	16.6371 ± 0.0005	113.3308 ± 0.0004	36.9206 ± 0.0003	142.7388 ± 0.0002	3.1859 ± 0.0002	5.1090 ± 0.0001	0.1773 ± 0.0002
S3	GaN	15.5764 ± 0.0001	113.5555 ± 0.0002	36.1796 ± 0.0001	143.3300 ± 0.0001	3.1840 ± 0.0001	5.1891 ± 0.0001	—
	AlInN	16.2062 ± 0.0007	113.3708 ± 0.0006	36.6014 ± 0.0005	142.9100 ± 0.0004	3.1838 ± 0.0002	5.1381 ± 0.0001	0.2012 ± 0.0002
S4	GaN	16.0653 ± 0.0001	114.0412 ± 0.0001	36.6681 ± 0.0001	143.8119 ± 0.0001	3.1846 ± 0.0001	5.1887 ± 0.0001	—
	AlInN	16.4884 ± 0.0008	113.9168 ± 0.0006	36.9546 ± 0.0004	143.5226 ± 0.0002	3.1861 ± 0.0002	5.1537 ± 0.0001	0.2168 ± 0.0002

J. Phys. D: Appl. Phys. **56** (2023) 245102
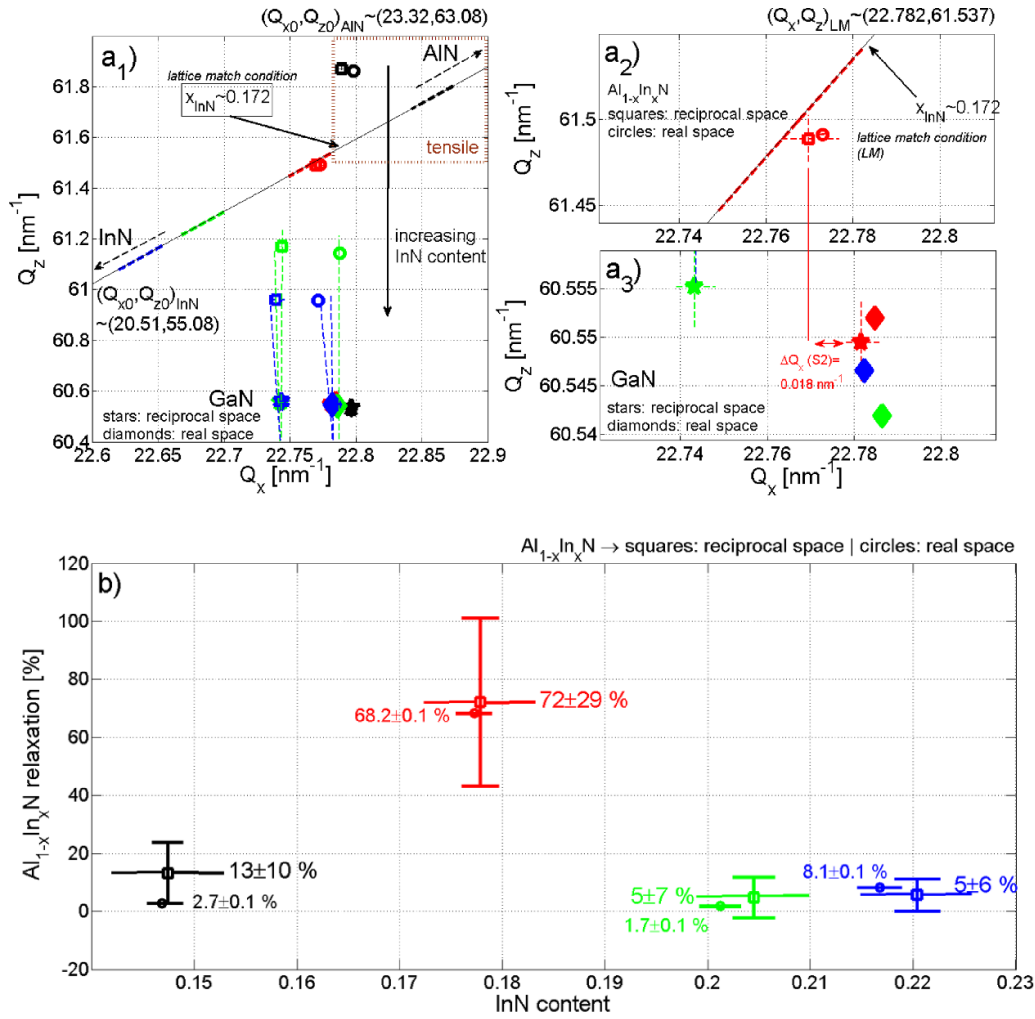
S Magalhães *et al*

Figure 2. (a_1) Representation in the reciprocal space of the measured $10\bar{1}5$ GaN and $Al_{1-x}In_xN$ diffraction spots indicating the $R = 1$ theoretical relaxed $(Q_x, Q_z) = (Q_{x0,AlN,InN}, Q_{z0,AlN,InN})$ pair of coordinates for every x_{InN} content from $x = 0$ (pure AlN) to $x = 1$ (pure InN)—black curve. With respect to the GaN/$Al_{1-x}In_xN$ diffraction spots, the stars and diamonds/squares and circles refer to the lattice units calculated directly by reciprocal space mapping and converted from real-space units to reciprocal lattice units, respectively. As evidenced in figure 1, higher InN contents are reflected in lower Q_z units. The $Al_{1-x}In_xN$ (Q_x, Q_z) pairs for the tensile compound are also highlighted. Magnifications around the relevant reciprocal lattice units derived for sample S2 (in red) are highlighted in figures (a_2) and (a_3), for the $Al_{1-x}In_xN$ compound and GaN, respectively. (b) Comparison between the relaxation degrees of the S series samples derived using a- and c-GaN and $Al_{1-x}In_xN$ lattice parameters calculated through reciprocal space mapping and real-space methodologies.

The vertical line that passes through the substrate (or thick GaN template) and the film, $Q_{\hat{x}\text{substrate}} = _\text{film}$ represents the pseudomorphic line, often designated as the fully strained line. In the case of the $Al_{1-x}In_xN$ compound, the ability to engineer the film's strain state from tensile to compressive through the incorporation of InN into the compound foresees a particular composition where the ternary is fully relaxed and at the same time pseudomorphic (or nearly pseudomorphic) to the GaN template. Therefore, although the vertical line anticipates pseudomorphic behaviour, at a particular '*magic*' lattice match condition the ternary is not fully strained but fully relaxed, instead. On the one hand, the green and blue lines in figure 2(a_1) passing through the $10\bar{1}5$ GaN as well as the $Al_{\sim0.795}In_{\sim0.205}N$ and $Al_{\sim0.779}In_{\sim0.221}N$ reciprocal lattice points, i.e. samples S3 and S4, respectively, evidence high levels of strain imposed by the binary. On the other hand, the $(Q_{\hat{x}}, Q_{\hat{z}}) = (22.7698, 61.4886)$ coordinates derived

for the ternary of sample S2 ($Al_{\sim0.822}In_{\sim0.178}N$) are very close to the ones calculated for a fully relaxed compound $((Q_{x0}, Q_{z0})_{Al(1-x)In(x)N} = (22.76, 61.48))$ with the same chemical composition. Thus, the ternary in sample S2 is almost relaxed whilst the other three layers are highly strained. Also depicted in figure 2(a_1) are the calculated $Al_{1-x}In_xN$ (Q_x, Q_z) pairs that lead the compound towards a tensile state if grown on top of a standard GaN template. Figures 2(a_2) and (a_3) allow observing in high detail the relevant reciprocal lattice units derived for sample S2 (in red) with respect to the $Al_{1-x}In_xN$ compound and GaN, respectively. The determination of the relaxation degree of the compound depends on the (Q_x, Q_z) coordinates for a fully relaxed $Al_{1-x}In_xN$ ($R = 1$) with a specific InN content (x) and the ternary's $(Q_{\hat{x}}, Q_{\hat{z}})$ diffraction centre.

Moreover, the uncertainty in the relaxation degree evidenced in figure 2(b)) is determined by considering the InN

molar fraction uncertainties in the calculation of the relaxed $Al_{1-x}In_xN$ *a*- and *c*-lattice parameters. The uncertainties in the GaN and $Al_{1-x}In_xN$ lattice parameters are converted to Q_x and Q_z units and represented in figure 2(a)) by horizontal and vertical dashed lines, respectively. Therefore, the relaxation degree may be determined as the angle between the vertical line (constant Q_x) that crosses the $Al_{1-x}In_xN$ $(Q_{\widehat{x}}, Q_{\widehat{z}})$ diffraction spot and the $R = 1$ line. A Monte Carlo algorithm generates 30 000 combinations of different $(Q_{\widehat{x}} \pm \Delta Q_{\widehat{x}}, Q_{\widehat{z}} \pm \Delta Q_{\widehat{z}})_{GaN/Al1-xInxN}$ and calculates the relaxation degree in each combination. The absolute value shown in figure 2(b)) is derived as the calculated average relaxation while the uncertainty corresponds to the standard deviation. The high dispersion for the relaxation of the compound may be also concluded geometrically from figure 2(a_1) by connecting the $Q_{\widehat{x}} + Q_{\widehat{x}}$ for GaN with the $Q_{\widehat{x}} - Q_{\widehat{x}}$ for $Al_{1-x}In_xN$ reciprocal lattice point (vertical and oblique dash-dashed lines). Calculating $Q_{\widehat{x}}$ for sample S2 as $(Q_{\widehat{x},Al_{0.178}In_{0.822}N} + \Delta Q_{\widehat{x},Al_{0.178}In_{0.822}N}) - (Q_{\widehat{x},GaN} - \Delta Q_{\widehat{x},GaN})$ results in $\sim 0.000\,17$ Å in real-space units. Therefore, considering the minimum Q_x for GaN and the maximum for the ternary, the $Al_{1-x}In_xN$ is nearly pseudomorphic to the binary because the difference in the in-plane lattice parameters is close to zero while a reasonable relaxation is found considering $(Q_{\widehat{x},Al_{0.178}In_{0.822}N} - \Delta Q_{\widehat{x},Al_{0.178}In_{0.822}N}) - (Q_{\widehat{x},GaN} + \Delta Q_{\widehat{x},GaN})$, i.e. $|Q_{\widehat{x}}| = 0.0253$ nm^{-1} or 0.0035 Å. The difference in the in-place lattice parameters in the latter case is only slightly higher if compared to the cases of samples S1 (0.0172 nm^{-1}), S3 (0.0108 nm^{-1}) and S4 (0.0118 nm^{-1}), respectively. Thus, sample S2 is found to be the one with a higher degree of relaxation as shown in figures 2(a_2) and (a_3). The uncertainty in the InN content is also represented in figure 2(b). Therefore, the uncertainties in the $Al_{1-x}In_xN$ relaxation degree and also in the InN content (via the uncertainties in the *a*- and *c*-lattice parameters) are quite high. The high uncertainty for the relaxation degree in the sample grown close to lattice matched conditions (S2) is unexpected and probably caused by some growth-related issues leading to different defect distributions in the interface and film. Nevertheless, it will not affect the analysis procedure presented here. From the data derived using the reciprocal space mapping, the only conclusions possible to be ascertained are related to the different InN molar fractions deduced for the four samples and the clear different relaxation degree of the $Al_{1-x}In_xN$ from sample S2. The procedure to calculate the $Al_{1-x}In_xN$ relaxation degree via the real-space method follows.

The $10\bar{1}4^{+/-}$ and $0004^{+/-}$ GaN and the $Al_{1-x}In_xN$ asymmetric and symmetric ω-scans from samples S1 to S4 are shown in figures 3(a_1, b_1, c_1, d_1) and (a_2, b_2, c_2, d_2), respectively. The simulated curves also included in the figure are optimized through symmetric PV functions. The difference between the ω-scans centroids simulated using a symmetric and an asymmetric PV is below the uncertainty of the former. The level of asymmetry calculated for the ω-scans is below 1%. The combined effect of the instrumental function, low levels of composition/strain heterogeneities, crystal mosaicity and

wafer curvature is suggested to play a minor role in the accuracy of the determination of the Bragg's peak centroid. The fits employing PVs show high agreement with the experimental data. The FWHMs are highlighted in inset figure 3. Considering the 4 measured reflections, the average FWHM are 0.108 ± 0.014° and 0.126 ± 0.003° for the GaN and the $Al_{1-x}In_xN$ films, respectively. Thus, as the GaN averaged FWHM is $\sim 17\%$ lower than the ternary's one, the bulk- and GaN templates present slightly better crystalline quality if compared to the deposited ternary. The deterioration of the crystalline quality observed in the ternary may be due to the morphology and nature of defects as observed by several authors [5, 60–62]. In fact, hillocks and V-pits are common in $Al_{1-x}In_xN$ layers. Although, it is not expected the formation of extra threading dislocations compared to the ones present at the GaN template, the extended defects usually are created at the sapphire/GaN interface and propagate towards the surface where they frequently terminate with V-type artefacts. Furthermore, the higher standard deviation calculated for the GaN is attributed to the higher dispersion of the FWHM derived for the binary. Indeed, the FWHM calculated for the bulk-GaN sample (S1) is $\sim 33\%$ lower if compared to the FWHMs of the thick S2, S3 and S4 GaN templates. The in- and out-of-plane lattice parameters were derived through Bond's method [31]. In Bond's method, as exhaustively described on S1, the *c*-lattice parameter is proportional to the angular separation in the real-space between 0004^+ and 0004^- centres ($\Delta\omega_{0004}$) while the *a*-lattice parameter depends on the angular spacing between the $10\bar{1}4^+$ and $10\bar{1}4^-$ Bragg peaks ($\Delta\omega_{10\bar{1}4}$) as well. $\Delta\omega_{0004}$ and $\Delta\omega_{10\bar{1}4}$ are indicated in figure 3. The optimized diffraction centres are depicted in figure 3 and in table 2.

The average GaN *a*- and *c*- lattice parameters are found to be 3.183 84 Å and 5.189 09 Å with 0.000 87 Å and 0.000 86 Å as the standard deviations. According to table 2, differences in $a_{Al_{1-x}In_xN}$ (RSM)$-a_{Al_{1-x}In_xN}$ (Bond) of 0.0012 Å (S1), 0.0004 Å (S2), 0.0061 Å (S3) and 0.0044 Å (S4) and $c_{Al_{1-x}In_xN}$ (RSM)$-c_{Al_{1-x}In_xN}$ (Bond) of -0.0006 Å (S1), 0.0002 Å (S2), -0.0022 Å (S3) and 0.0001 Å (S4) between the *a*- and *c*- lattice parameters of the $Al_{1-x}In_xN$ derived via the reciprocal space mapping and Bond's real space method are, respectively, found. On the one hand, for samples S3 and S4, the above differences between the derived *a*-lattice parameters (in modulus) are found to be higher than the uncertainties in the respective $a_{Al_{1-x}In_xN}$ lattice parameters derived by the former method (the method with higher uncertainties). On the other hand, sample S3 evidences higher $c_{Al_{1-x}In_xN}$ (RSM)$-c_{Al_{1-x}In_xN}$ (Bond) than $\Delta c_{AlInN\ RSM}$ but within the margin of uncertainty if compared to $|\Delta c_{AlInN\ RSM}(S3) + \Delta c_{AlInN\ Bond}(S3)| = 0.0021 + 0.0001$. In fact, the uncertainties in the lattice parameters calculated through the real-space method are at least one order of magnitude smaller if compared to the same quantity derived via reciprocal space mapping (see table 2). The uncertainty in the *a*- lattice parameter (Δa) determined through the real space method is a function of $\frac{\partial a}{\partial \lambda}\Delta\lambda$, $\frac{\partial a}{\partial \omega_{h0\bar{h}l}^{+/-}}\Delta\omega_{h0\bar{h}l}^{+/-}$, $\frac{\partial a}{\partial c}\Delta c$ and $\frac{\partial a}{\partial d}\Delta d$ while the uncertainty in the *c*- lattice parameter (Δc)
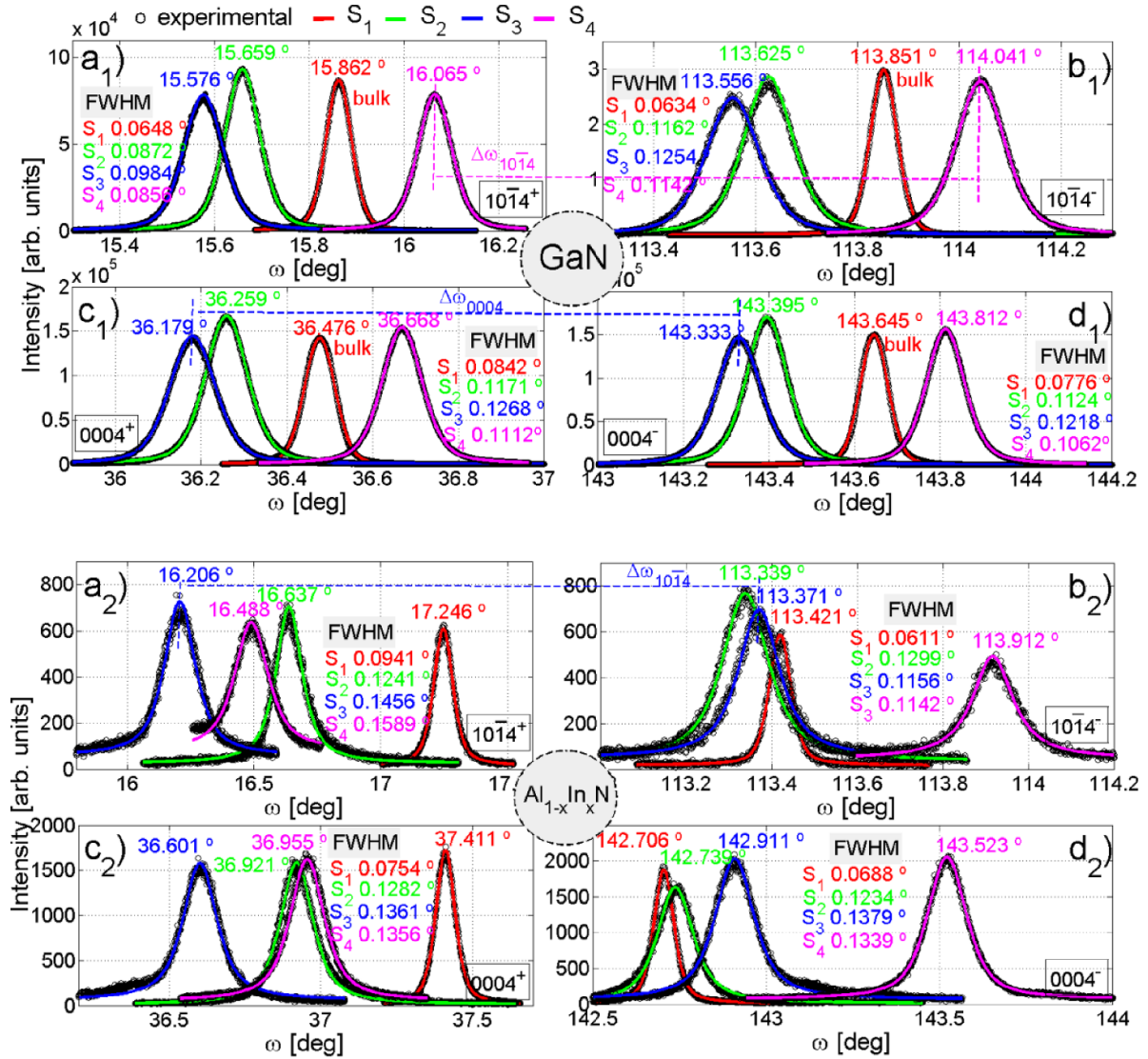
Figure 3. Experimental ω-scans around the $10\bar{1}4^{+/-}$ GaN/Al$_{1-x}$In$_x$N asymmetrical (a$_{1/2}$, b$_{1/2}$) and symmetrical $0004^{+/-}$ GaN (c$_{1/2}$, d$_{1/2}$) reflections as well as the respective fittings employing a Pseudo-Voigt function. Insets show the optimized centres and the derived FWHM. The red lines in figures (a$_1$)–(d$_1$) refer to PV fitting of the 4ω-scans with respect to the bulk-GaN while (a$_2$)–(d$_2$) address the PV fittings of the ternary compound grown on top of the bulk-GaN.

depends on $\frac{\partial c}{\partial \lambda}\Delta\lambda$, $\frac{\partial c}{\partial \omega_{000l}^+}\Delta\omega_{000l}^{+/-}$. According to the diffractometer manufacturer $\Delta\lambda = 3.8 \times 10^{-6}$ Å. Moreover, $\Delta\omega_{h0\bar{h}l}^+$, $\Delta\omega_{h0\bar{h}l}^-$, $\Delta\omega_{000l}^+$ and $\Delta\omega_{000l}^-$ are the errors in the incident angles output by the Marquardt–Levenberg fitting algorithm for the $\omega_{h0\bar{h}l}^{+/-}$, $\omega_{h0\bar{h}l}^-$, ω_{000l}^+ and ω_{000l}^- diffraction centres [63]. The first term in Δa and Δc are found to represent less than 1% of the total uncertainty while the uncertainties related to $\Delta\omega_{h0\bar{h}l}^{+/-}$ and to $\Delta\omega_{000l}^{+/-}$ contain around $\sim$99% of the total uncertainty distributed between the effect of Δc and Δd in the in-plane lattice parameter and $\sim$99% for the orthogonal direction. Exhaustive description of the calculation of the uncertainties in the lattice parameters is addressed in S1. The differences in the in-plane lattice parameters between the ternary and the binary in the real-space method are -0.0002 Å (S1), 0.0017 Å (S2), -0.0002 Å (S3), 0.0015 Å (S4). Therefore,

Δa_{Bond} derived using Bond's method are in the same magnitude order as Δa_{RSM}. Although the differences between the derived Al$_{1-x}$In$_x$N a-lattice parameters calculated via the reciprocal and real-space methods are outside the sum of the individual uncertainties for $a_{\text{Al}1-x\text{In}x\text{N}}$ in samples S3 and S4, the same order of magnitude in Δa_{Bond} and Δa_{RSM} suggest small-misalignments at the reciprocal space method measurements. The ternaries present in S1 and S3 samples reveal the highest level of pseudomorphism suggesting negligible dependency of Δa_{Bond} with the InN content in the range of $0.1469 < x\text{InN} < 0.2168$. Converting a- and c-lattice parameters to reciprocal space units allows comparing the relaxation degree derived by both methodologies. As evidenced in figure 2(b), the relaxation degrees of the Al$_{1-x}$In$_x$N layers derived through real-space methodology agree inside the uncertainties with the ones derived by reciprocal space

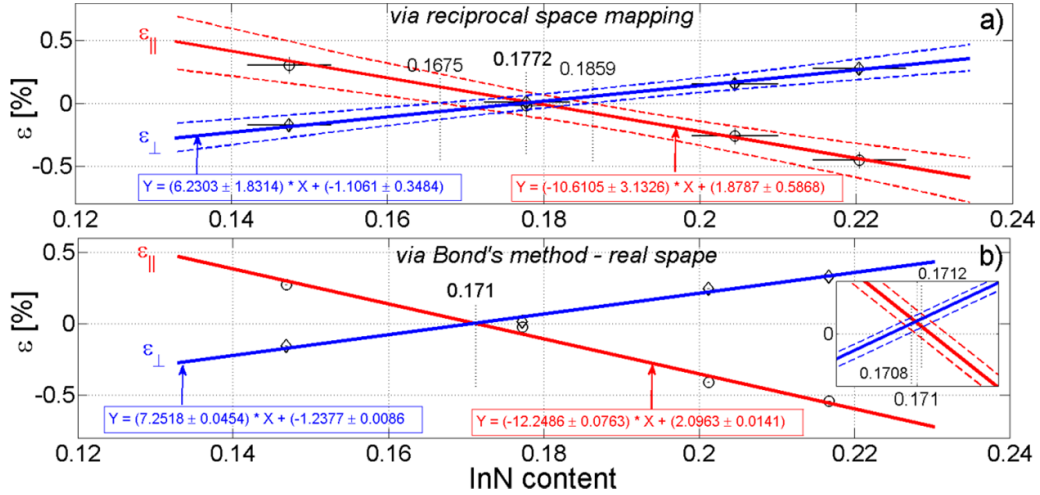**Figure 4.** Parallel ($\varepsilon_{||}$) and perpendicular ($\varepsilon_{\perp}$) deformations as a function of the InN content and calculated using the *a*- and *c*- GaN and Al$_{1-x}$In$_x$N lattice parameters derived via the reciprocal space mapping, (a), and the real-space Bond's method, (b). Around $x_{InN} = 0.171$ a magnification is highlighted to illustrate the lower uncertainties for both orthogonal deformations if derived through the real-space methodology.

mapping. Concretely, the relaxation degrees are found to be $13 \pm 10\%$, $72 \pm 29\%$, $5 \pm 7\%$, and $5 \pm 6\%$ for the former while $2.7 \pm 0.1\%$, $68.2 \pm 0.1\%$, $1.7 \pm 0.1\%$ and $8.1 \pm 0.1\%$ are calculated employing the latter method. Therefore, if the Bragg peaks from the film are not overlapped or partially overlapped with the ones from the substrate, then Bond's method or any other real-space method is preferable in order to derive the film's relaxation degree.

Finally, the '*magic*' lattice match condition may be obtained analytically through the calculation of the parallel and perpendicular to the sample surface deformations defined by $\varepsilon_{||} = \frac{a_{Al_{1-x}In_xN} - a_0(x)}{a_0(x)}$ and $\varepsilon_{\perp} = \frac{c_{Al_{1-x}In_xN} - c_0(x)}{c_0(x)}$, respectively. $a_0(x)$ and $c_0(x)$ are the relaxed lattice parameters for a given InN content, x. Figure 4(a) evidences and $\varepsilon_{\perp}$ as functions of the InN content for the 4 analysed samples via reciprocal space mapping while figure 4(b) represents the same evolution using the lattice parameters and chemical composition determined by the real space Bond's method. As observed in figures 2(b) and in 4(a), (b), the InN contents derived by reciprocal and real-spaces lie inside the uncertainties found in the respective methodologies. In fact, according to table 2, the InN contents are found to be 0.1474 ± 0.0053 (S1), 0.1778 ± 0.0055 (S2), 0.2045 ± 0.0055 (S3) and 0.2204 ± 0.0059 (S4) and 0.1469 ± 0.0002 (S1), 0.1773 ± 0.0002 (S2), 0.2012 ± 0.0002, 0.2012 ± 0.0002 (S3) and 0.2168 ± 0.0002 (S4), derived through the reciprocal- and real-space methods, respectively. By not including refraction correction in the calculations, the derived absolute xInN contents decreases to 0.1468 (S1), 0.1772 (S2), 0.2011 (S3) and 0.2167 (S4), respectively. In fact, refraction correction affects only slightly the optimized ω-scan centre by a certain amount close to $-0.001°$. Nevertheless, the *a*- and *c*-lattice parameters are calculated considering $\Delta\omega_{10\bar{1}4}$ and $\Delta\omega_{0004}$ as depicted in figure 3 which are only slightly affected. Considering sample S3 as an example, $\Delta\omega_{10\bar{1}4}$ decreases an amount of 0.0003° and

0.0001° resulting in a difference below 0.01% in the calculated InN content if one considers refraction correction or not (0.1473–0.1472).

The linear regression equation takes into account the uncertainties of the fitting parameters. Therefore, it considers the Δx_{InN}, $\Delta\varepsilon_{||}$, and $\Delta\varepsilon_{\perp}$. In order to determine Δx_{InN} the method used here considers the propagation of the lattice parameter uncertainties, i.e. for $a \pm \Delta a$ and $c \pm \Delta c$ as well as the uncertainties of the AlN and InN relaxed lattice parameters and the respective stiffness coefficient uncertainties of 0.001 Å and 5 GPa. A maximum and a minimum $x_{crystal}$ are calculated. Then, $\Delta x_{crystal} = \frac{\max(x_{crystal}) - \min(x_{crystal})}{2}$. A Monte Carlo algorithm to derive the hyperbolic boundary curves represented by dashed lines in figure 4(a) and the inset of 4(b) is used in the fitting procedure. The uncertainty in the fitting parameters is computed in 5000 iterations, assuming that errors are Gaussian and centred. The linear fitting procedure yields $y_{RSM}(\varepsilon_{||}) = m_{RSM}x + b_{RSM} = (-10.6105 \pm 3.1326)x + (1.8787 \pm 0.5868)$ and $y_{real}(\varepsilon_{||}) = m_{real}x + b_{real} = (6.2303 \pm 1.8314)x + (-1.1061 \pm 0.34843)$ for $\varepsilon_{||}$ and $y_{RSM}(\varepsilon_{\perp}) = m_{RSM}x + b_{RSM} = (-12.2486 \pm 0.076349)x + (2.0963 \pm 0.014104)$ and $y_{real}(\varepsilon_{\perp}) = m_{real}x + b_{real} = (7.2518 \pm 0.04539)x + (-1.2377 \pm 0.0086111)$ for $\varepsilon_{\perp}$, respectively. On the one hand, the absolute lattice match condition is found when $y_{RSM}(\varepsilon_{||}) = y_{RSM}(\varepsilon_{\perp})$ and $y_{real}(\varepsilon_{||}) = y_{real}(\varepsilon_{\perp})$ with $\Delta m \to 0$ and $\Delta b \to 0$ resulting in 0.1772 and 0.1710, derived via reciprocal and real-spaces, respectively. On the other hand, the lower hyperbolic curve marked in figure 4(a) and in the inset of figure 4(b) and determined for $\varepsilon_{||}$ crosses the upper one found for $\varepsilon_{\perp}$ at 0.1675/0.1708 while the upper hyperbolic curve derived for $\varepsilon_{||}$ crosses the lower hyperbolic curve determined for $\varepsilon_{\perp}$ at 0.1859/0.1712 for the reciprocal/real space, respectively. The above values constitute the InN content boundaries found with a 95% confidence level. To conclude

the section, the impact of the findings from a technological point of view may be tremendous. In fact, the interval $\sim 1.8\%$ (0.1859–0.1675) of InN content found via reciprocal space mapping for the lattice match condition of $Al_{1-x}In_xN$ grown on GaN templates (or substrate) is quite high, contrary to the 0.04% determined through Bond's method. It is interesting to note a 41 times decrease in the ratio between the uncertainties derived via both methods for the slope and curve offset with respect of $\varepsilon_{||}$ and $\varepsilon_\perp$, respectively. Finally, on the one hand, the uncertainty in the relaxation degree of the $Al_{1-x}In_xN$ depends on the uncertainties in the lattice parameter of the ternary and the ones from the GaN template/substrate as well. On the other hand, uncertainties in $\varepsilon_{||}$ and $\varepsilon_\perp$ depend on the uncertainties of the $Al_{1-x}In_xN$ measured lattice parameters and the ones from the relaxed ternary, calculated using Vegard's rule. Therefore, the uncertainties in $\varepsilon_{||}$ and $\varepsilon_\perp$ depend on the uncertainties in the GaN lattice parameters only indirectly. Thus, the uncertainty in the determined '*magic*' lattice condition is almost independent of the uncertainties in the GaN lattice parameters because the $Al_{1-x}In_xN$ lattice parameters do not depend analytically on the binary's lattice parameters but the uncertainties of the binary are fundamental to calculate the relaxation degree of the ternary.

3.2. Germanium tin films grown on germanium virtual substrates (cubic)

The relaxation degree of two sets of $Ge_{1-x}Sn_x$ films grown on Ge virtual substrates by MBE (C series) and CVD (A series) are derived and compared. Figure 5 shows the Si (a_1 to d_1), Ge (a_2 to d_2) and $Ge_{1-x}Sn_x$ (a_3 to d_3) $115^{+/-}$ and $004^{+/-}$ experimental ω-scans of the C1, C2 and C3 samples together with the simulations by employing PVs. As in the case of the group-III nitrides, the ω-scans were also simulated using asymmetric PVs and very low levels of asymmetry were deduced. Therefore, the determination of the lattice parameters of the Si, Ge and the $Ge_{1-x}Sn_x$ considers the centre of the $115^{+/-}$ and $004^{+/-}$ experimental ω-scans calculated via a symmetric PV. The 4 Miller indexes used in the previous section are replaced by a set of 3 Miller indexes, more appropriate for the measured reflections in cubic crystals. The optimized ω-scan centres for the individual Bragg peaks as well as the respective FWHM calculated for the heterostructure are depicted in inset figure 5 and summarized in table 3. As in the case of the nitride semiconductors, the PV fittings reproduce accurately the experimental ω-scans. As expected, the FWHMs indicate better crystalline quality attributed to the Si while the $Ge_{1-x}Sn_x$ reveals similar broadenings amongst each sample and compared to the Ge virtual substrate as well. Furthermore, the asymmetry in 115^+ $Ge_{0.962}Sn_{0.038}$ (C1) ω-scan highlighted in figure 5(a_3) suggested to be due to strain and/or composition heterogeneities agrees with the results determined via RSM in [1] where a detailed analysis of reciprocal space mapping of the current samples was engaged. The inter-planar distance of a cubic crystal only depends on one lattice parameter through $\frac{1}{d^2} = \frac{h^2+k^2+l^2}{a^2}$. Therefore, in order to study the effect of the strain on the epitaxial growth, the Si, Ge and Sn unit

cells are treated mathematically as tetragonal cells, instead of the typical cubic. In fact, the tetragonal cell converges to a cubic one when $a \equiv b \equiv c$. In a tetragonal cell, $\frac{1}{d^2} = \frac{h^2+k^2}{a^2} + \frac{l^2}{c^2}$ thus, $a_{||} \equiv a$ and $a_\perp \equiv c$ may be determined independently. The $a_{||}$ and $a_\perp$ lattice parameters depicted in table 3 are calculated from the angular separation between the optimized 115^+ and 115^- ($\Delta\omega_{115}$) and the 004^+ and 004^- ($\Delta\omega_{004}$), respectively. The $a_{||}/a_\perp$ derived via the real-space method are 5.4316 Å/5.4308 Å, 5.6592 Å/5.6606 Å, 5.6699 Å/5.6826 Å for sample C1, 5.4306 Å/5.4313 Å, 5.6491 Å/5.6662 Å, 5.6648 Å/5.7059 Å for sample C2 and 5.4312 Å/5.4313 Å, 5.6519 Å/5.6646 Å, 5.6671 Å/5.7122 Å for sample C3. The three sets of values refer to the Si substrate, the Ge template and the $Ge_{1-x}Sn_x$ layers, respectively. From the derived lattice parameters, Sn contents of 0.0227 ± 0.0003, 0.0405 ± 0.0002 and 0.0384 ± 0.0003 are determined via the real-space method while 0.017 ± 0.005, 0.040 ± 0.004, and 0.042 ± 0.006 were previously found through the reciprocal-space method [1]. Therefore, perfect agreement in the Sn contents between methods is found.

In order to obtain the relaxation degree of the CVD $Ge_{1-x}Sn_x$ layers and compare with the same for the MBE $Ge_{1-x}Sn_x$ ones, the first step is to determine the lattice parameters and respective uncertainties of the tin compound as well as of the Ge virtual substrate via reciprocal and real-space methods. Figure 6 shows the experimental RSM around the Si, Ge (CVD) and $Ge_{1-x}Sn_x$ (CVD) 115 reciprocal lattice points. As in the case of the group-III nitrides, no other truncation rod was observed rather than the ones associated to the diffraction of the Si, Ge and the $Ge_{1-x}Sn_x$ films. The absence of a vertically elongated diffraction spot suggests a low density of misfit dislocations. The simulations using 2D-Gaussians perfectly agree with the data and are included on the right side of each measurement. In figure 6, the three horizontal dash-dot lines (along Q_z) cross the 115 Si, 115 Ge and the 115 $Ge_{0.932}Sn_{0.068}$ diffraction spots, respectively. The former two Q_z lines suggest similar out-of-plane Si and Ge lattice parameters ($a_\perp$) among the three samples while the lower Q_z line, associated to the tin compound, reveals decreasing Q_z centroid, thus, increasing $a_\perp$. Therefore, the tin incorporation increases from the left to the right in figure 6. Specifically, compositions of $Ge_{0.932}Sn_{0.068}$, $Ge_{0.906}Sn_{0.094}$, $Ge_{0.877}Sn_{0.123}$ are found for samples A1, A2 and A3, respectively. Moreover, the broadenings along Q_x and Q_z directions ($\delta Q_x, \delta Q_z$) are much higher in the 115 Ge and 115 $Ge_{1-x}Sn_x$ than in the 115 Si diffraction spots. In fact, the ($\delta Q_x, \delta Q_z$) for the various samples are $(0.0526, 0.0750)$ nm^{-1}, $(0.3800, 0.2000)$ nm^{-1} and $(0.3729, 0.1663)$ nm^{-1}, $(0.0573, 0.0800)$ nm^{-1}, $(0.3000, 0.1736)$ nm^{-1} and $(0.3646, 0.2002)$ nm^{-1}, and $(0.0550, 0.0645)$ nm^{-1}, $(0.1700, 0.1350)$ nm^{-1} and $(0.2700, 0.1600)$ nm^{-1}, for the Si, Ge and $Ge_{1-x}Sn_x$, respectively. Also interesting to note is the splitting of the 115 $Ge_{1-x}Sn_x$ with xSn = 0.094 (sample A2) diffraction spot while on the other two samples higher symmetry is observed. In fact, as observed in MBE $Ge_{1-x}Sn_x$ layers grown on Ge buffers and reported in [24] compositional heterogeneities are expected even for low Sn contents.

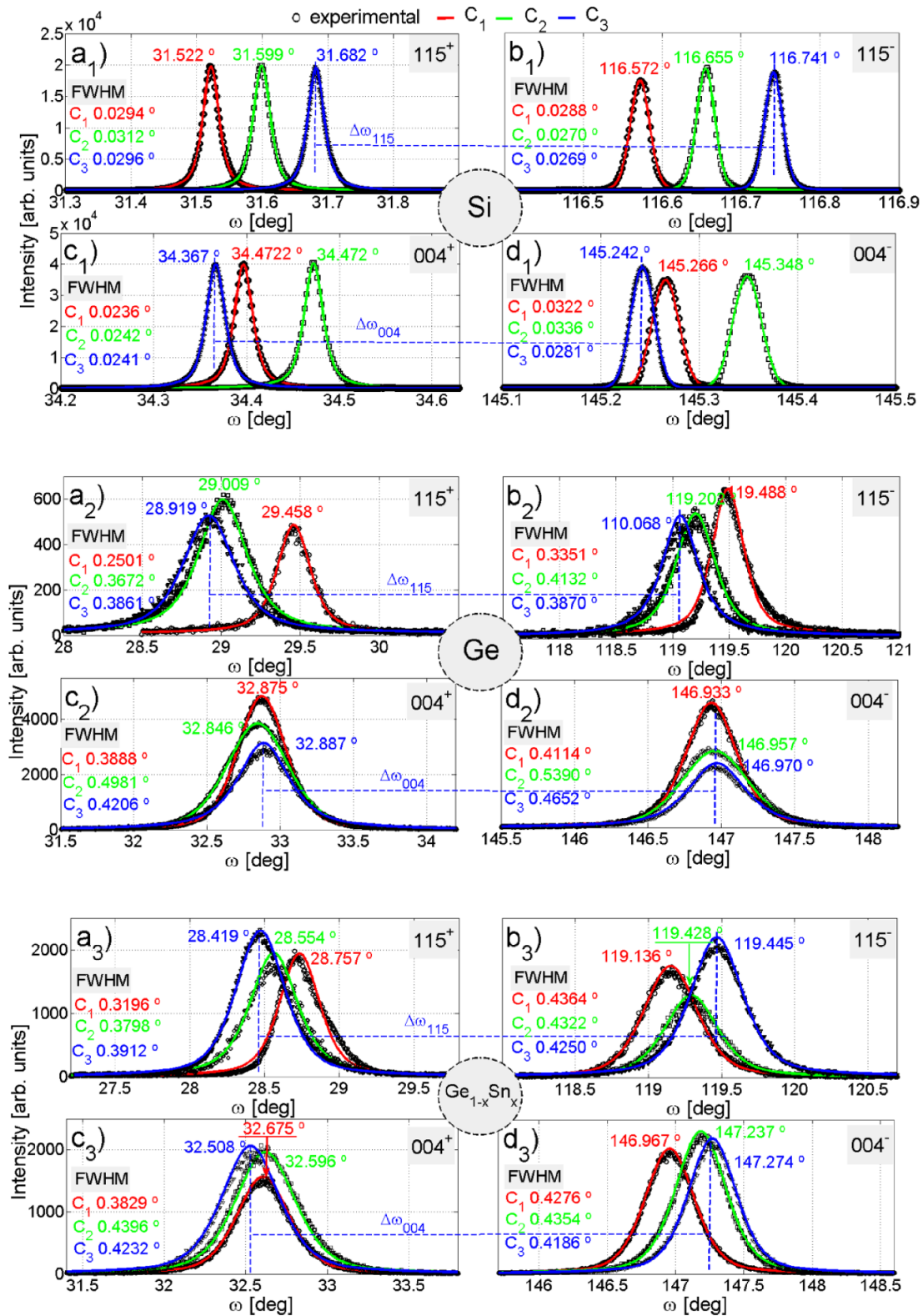**Figure 5.** Experimental ω-scans around the $115^{+/-}$ Si, Ge, $Ge_{1-x}Sn_x$ asymmetrical (a$_{1/2}$, b$_{1/2}$, c$_{1/2}$) and symmetrical $004^{+/-}$ (a$_{3/4}$, b$_{3/4}$, c$_{3/4}$, d$_{3/4}$,) reflections as well as the respective fittings employing Pseudo-Voigt functions, respectively. Insets show the diffraction curves optimized centres and the derived FWHM. Case of the tin compounds grown by MBE.

The RSMs from figure 6 as well as $a_{||}$ and $a_{\perp}$ depicted in table 4 for the Si, Ge and $Ge_{1-x}Sn_x$ crystals suggest strain and composition heterogeneities to be present in the CVD tin compounds. As a matter of fact, $a_{||,Ge_{1-x}Sn_x}$ appears to be slightly higher (lower $Q_{\hat{z}}$ centroid) than the same for the Ge indicating partial relaxation in the former. At the same

Table 3. C1 to C3 Si, Ge and Ge$_{1-x}$Sn$_x$ in-plane ($a_{||}$) and out-of-plane ($a_{\perp}$) -lattice parameters, calculated $\omega_{115}^{+/-}$ and $\omega_{004}^{+/-}$ centres and as well as the derived Sn contents calculated using the Ge and the Sn relaxed lattice parameters and respective uncertainties indicated in table 1. The relevant uncertainties are included. Poisson law was used together with Vegard's rule to determine the chemical composition. C series refer to the tin compounds grown by MBE.

| Sample	ω_{115}^{+} (deg)	ω_{115}^{-} (deg)	ω_{004}^{+} (deg)	ω_{004}^{+} (deg)	$a_{||}$ (Å)	$c \equiv a_{\perp}$ (Å)	Sn molar fraction
C1 (Si)	31.5217 ± 0.0001	116.5720 ± 0.0001	34.3965 ± 0.0001	145.2656 ± 0.0001	5.4316 ± 0.0001	5.4308 ± 0.0001	—
C1(Ge)	29.0889 ± 0.0013	119.2023 ± 0.0015	32.8462 ± 0.0006	146.9567 ± 0.0011	5.6592 ± 0.0005	5.6606 ± 0.0004	—
C1(GeSn)	28.7341 ± 0.0019	119.1520 ± 0.0001	32.6065 ± 0.0001	146.9568 ± 0.0001	5.6609 ± 0.0005	5.6826 ± 0.0004	0.0223 ± 0.0003
C2 (Si)	31.5992 ± 0.0001	116.6553 ± 0.0004	34.4722 ± 0.0001	145.3488 ± 0.0001	5.4306 ± 0.0001	5.4313 ± 0.0001	—
C2(Ge)	29.0889 ± 0.0013	119.2023 ± 0.0015	32.8462 ± 0.0001	146.9567 ± 0.0011	5.6491 ± 0.0004	5.6662 ± 0.0001	—
C2(GeSn)	28.5614 ± 0.0017	119.2935 ± 0.0011	32.6207 ± 0.0008	147.1848 ± 0.0007	5.6685 ± 0.0005	5.7009 ± 0.0001	0.0405 ± 0.0003
C3 (Si)	31.6819 ± 0.0001	116.7414 ± 0.0001	34.3667 ± 0.0001	145.2423 ± 0.0001	5.4312 ± 0.0005	5.4313 ± 0.0001	—
C3(Ge)	28.1876 ± 0.0015	119.9068 ± 0.0019	32.8865 ± 0.0015	146.9700 ± 0.0002	5.6519 ± 0.0005	5.6646 ± 0.0001	—
C3(GeSn)	28.4722 ± 0.0012	119.4678 ± 0.0009	32.5294 ± 0.0011	147.2687 ± 0.0006	5.6671 ± 0.0005	5.7122 ± 0.0001	0.0384 ± 0.0003
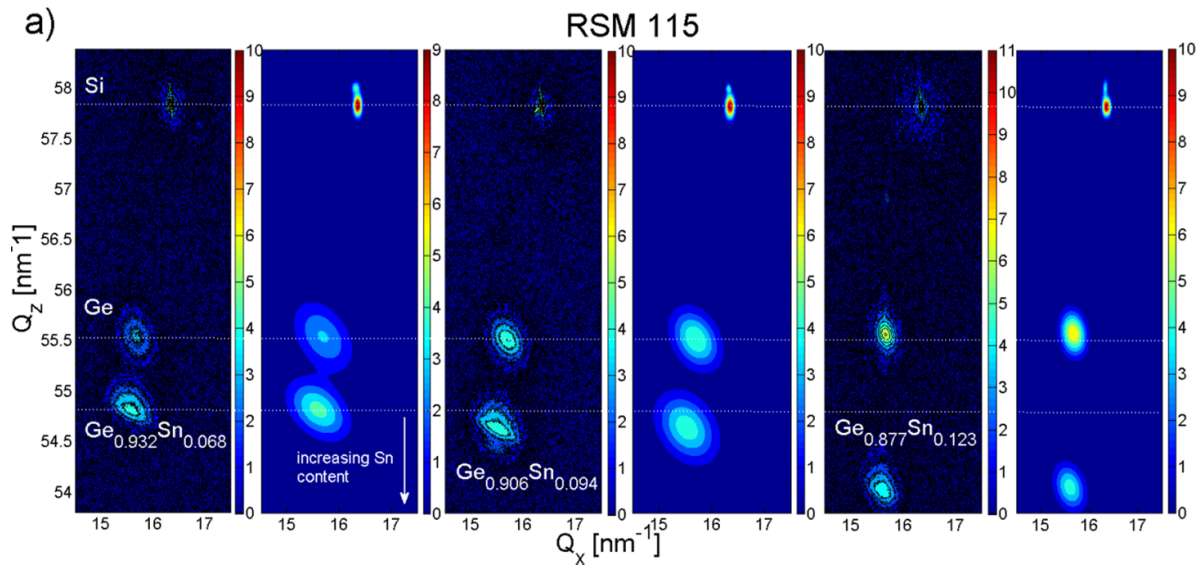
Figure 6. (a) Experimental (left diagrams) and simulated (right diagrams) using 2D-Gaussians reciprocal space maps around the 115 Si, Ge and Ge$_{1-x}$Sn$_x$ reciprocal lattice points for the 3 CVD Ge$_{1-x}$Sn$_x$ samples. The Ge$_{1-x}$Sn$_x$ Q_z decreases from left to right indicating higher lattice parameters, thus, higher Sn incorporation in the compound.

time $a_{\perp,\text{Ge}_{1-x}\text{Sn}_x}$ is higher than the equivalent for Ge supporting variations in the chemical composition in the three samples. High-resolution 004 2θ–ω scans around the Si, Ge and Ge$_{1-x}$Sn$_x$ peaks are accumulated and detailed analysis is addressed in S4. The simulations of the 004 2θ–ω scans were performed using the MROX software. MROX is a recognized code to simulate the 2θ–ω scans using the dynamical theory of XRD of any cubic, hexagonal, tetragonal, orthorhombic and monoclinic Bravais lattices [64–67]. From the simulations of the diffraction patterns the thickness of the Ge and the Ge$_{1-x}$Sn$_x$ are found to be 95 ± 10 nm and 295 ± 10 nm for A1 sample, 275 ± 10 and 200 ± 10 nm for A2 sample and 285 ± 10 nm and 100 ± 10 nm for A3 sample. The thicknesses of the individual layers agree perfectly with the ones expected by the nominal growing conditions.

Following the procedure described for the Al$_{1-x}$In$_x$N compounds, the Ge$_{1-x}$Sn$_x$ relaxation degree is calculated using the ($Q_{\hat{x}}$, $Q_{\hat{z}}$) optimized coordinates of the binary's and Ge's

diffraction spots as well as the reciprocal lattice units calculated for the relaxed film with a given chemical composition. In the case of the real-space methods, the lattice parameters are converted into reciprocal space units. The relaxation degree represented as a function of the Sn content derived using the real-space approach is compared with the one derived via space mapping in figures 7(a) and (b) for the MBE and CVD Ge$_{1-x}$Sn$_x$ layers, respectively. The former is represented using opened circles while the latter is depicted using opened squares.

Although the Sn contents derived via both methods agree inside respective uncertainties, the reciprocal-space method outputs approximately five times higher uncertainties for the chemical composition as evidenced in table 4. On the one hand, the drawback of employing the reciprocal space methodology is clear from the higher uncertainties (table 4). On the other hand, according to [1] sample C2 contains a double Ge$_{1-x}$Sn$_x$ layer with $x \sim 0.032$ and $x \sim 0.04$. The similar tin

Table 4. Si, Ge and Ge$_{1-x}$Sn$_x$ in-plane ($a_{||}$) and out-of-plane ($a_\perp$)-lattice parameters calculated $\omega_{115}^{+/-}$ and $\omega_{004}^{+/-}$ centres and as well as the derived Sn contents calculated using the Ge and the Sn relaxed lattice parameters and respective uncertainties indicated in table 1. The relevant uncertainties are also included. Poisson law was used together with Vegard's rule to determine the chemical composition.

Sample		$Q_{\tilde{x}}$ (nm^{-1})	$Q_{\tilde{z}}$ (nm^{-1})	a (Å)	c (Å)	Sn molar fraction
A1	Si	16.3556 ± 0.0024	57.8419 ± 0.0029	5.4327 ± 0.0001	5.4313 ± 0.0001	—
	Ge	15.6395 ± 0.0192	55.5375 ± 0.0286	5.6621 ± 0.0069	$56\,567 \pm 0.0029$	—
	GeSn	15.5984 ± 0.0144	54.8250 ± 0.0175	5.6966 ± 0.0053	5.7302 ± 0.0018	0.0685 ± 0.0068
A2	Si	16.3517 ± 0.0027	57.8458 ± 0.0034	5.4342 ± 0.0001	5.4310 ± 0.0001	—
	Ge	15.7015 ± 0.0111	55.5202 ± 0.0251	5.6592 ± 0.0039	5.6585 ± 0.0026	—
	GeSn	15.5310 ± 0.0134	54.6505 ± 0.0292	5.7213 ± 0.0049	5.7485 ± 0.0031	0.0941 ± 0.0071
A3	Si	16.3565 ± 0.0028	57.8491 ± 0.0024	5.4326 ± 0.0001	5.4307 ± 0.0001	—
	Ge	15.6768 ± 0.0074	55.5882 ± 0.0107	5.6682 ± 0.0027	5.6516 ± 0.0011	—
	GeSn	15.6041 ± 0.0129	54.0653 ± 0.0158	5.6945 ± 0.0048	5.8107 ± 0.0017	0.1228 ± 0.0106

| Sample		$\omega_{10\bar{1}5}^{+}$ (deg)	$\omega_{10\bar{1}5}^{-}$ (deg)	ω_{0004}^{+} (deg)	ω_{0004}^{-} (deg)	$a_{||}$ (Å)	c (Å)	Sn molar fraction
A1	Si27c	31.8076 ± 0.0001	116.8647 ± 0.0001	34.6979 ± 0.0001	145.5683 ± 0.0001	5.4274 ± 0.0005	5.4315 ± 0.0001	—
	Ge	$29.737\,93 \pm 0.0016$	119.3203 ± 0.0011	33.1278 ± 0.0016	147.1332 ± 0.0011	5.6557 ± 0.0005	5.6576 ± 0.0001	—
	GeSn	28.6011 ± 0.0018	119.9193 ± 0.0019	32.6812 ± 0.0007	147.6135 ± 0.0009	5.6951 ± 0.0005	5.7292 ± 0.0004	0.0694 ± 0.0003
A2	Si24b	31.5303 ± 0.0001	116.5809 ± 0.0001	34.4083 ± 0.0001	145.2821 ± 0.0001	5.4292 ± 0.0004	5.4311 ± 0.0001	—
	Ge	29.0798 ± 0.0009	119.0369 ± 0.0013	32.8399 ± 0.0005	146.8563 ± 0.0003	5.6561 ± 0.0005	5.6585 ± 0.0003	—
	GeSn	28.1509 ± 0.0013	119.8452 ± 0.0019	32.2792 ± 0.0008	147.4522 ± 0.0009	5.7191 ± 0.0005	5.7482 ± 0.0004	0.0924 ± 0.0003
A3	Si26c	31.3141 ± 0.0001	116.3714 ± 0.0001	34.1957 ± 0.0001	145.0745 ± 0.0001	5.4287 ± 0.0005	5.4315 ± 0.0001	—
	Ge	28.7894 ± 0.0003	118.6450 ± 0.0004	32.5063 ± 0.0002	146.4436 ± 0.0002	5.6630 ± 0.0005	5.6526 ± 0.0001	—
	GeSn	27.1241 ± 0.0009	119.9288 ± 0.0012	31.6647 ± 0.0009	147.6589 ± 0.0006	5.6866 ± 0.0005	5.8139 ± 0.0004	0.1208 ± 0.0003
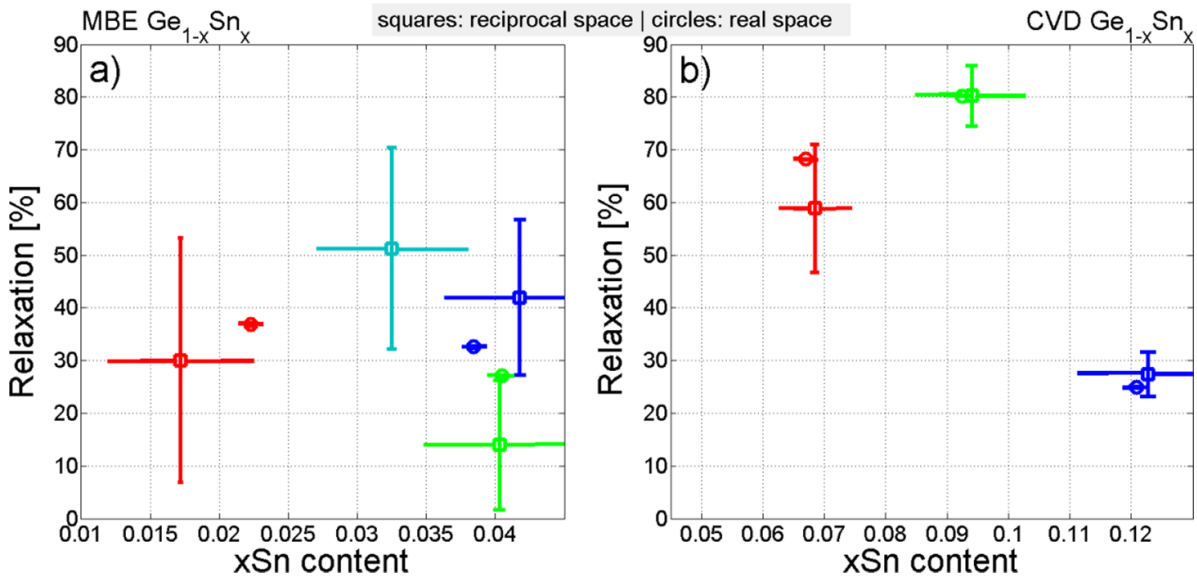
Figure 7. Comparison between the relaxation degrees derived using the Ge and Ge$_{1-x}$Sn$_x$ lattice parameters calculated through reciprocal space mapping and real-space methodologies, (a) MBE, (b) CVD, Ge$_{1-x}$Sn$_x$ layers.

content of both layers introduces ambiguities in the ω-scan measurements. In fact, similar Sn contents diffract the x-rays in close scattering angles (2θ) making it more difficult to separate both signals. Both tin contents marked with light blue and green open squares are included in figure 7(a). The uncertainties calculated for the relaxation degree for the Ge$_{1-x}$Sn$_x$ layers grown by MBE and CVD are at least one order of magnitude higher if derived by the reciprocal space method than the same calculated by Bond's method (real-space). Nevertheless, the relaxation degrees as well as the Sn contents derived through the two methods agree inside the errors. Figure 8 shows pie charts with the relative weight of the individual

components of Δd as well as $\frac{\partial a}{\partial d}\Delta d$ and the three independent parcels in Δc. It is concluded from figure 8 that the relative weight of terms containing the wavelength divergence ($\Delta\lambda$) overall total uncertainty is negligible and inferior to 1%. In fact, Δd is mainly dependent on the uncertainties in the ω-scan centroids of the asymmetric reflections while the uncertainties in the ω-scan centroids of the symmetric reflections dominate Δc. On the other hand, the dependency of Δc is found to be higher than the dependency of Δd in Δa. Moreover, figure 8 suggests negligible dependence of the crystallographic system and even on the growing technique in the relative weights of the different uncertainties. In fact, concerning the two different
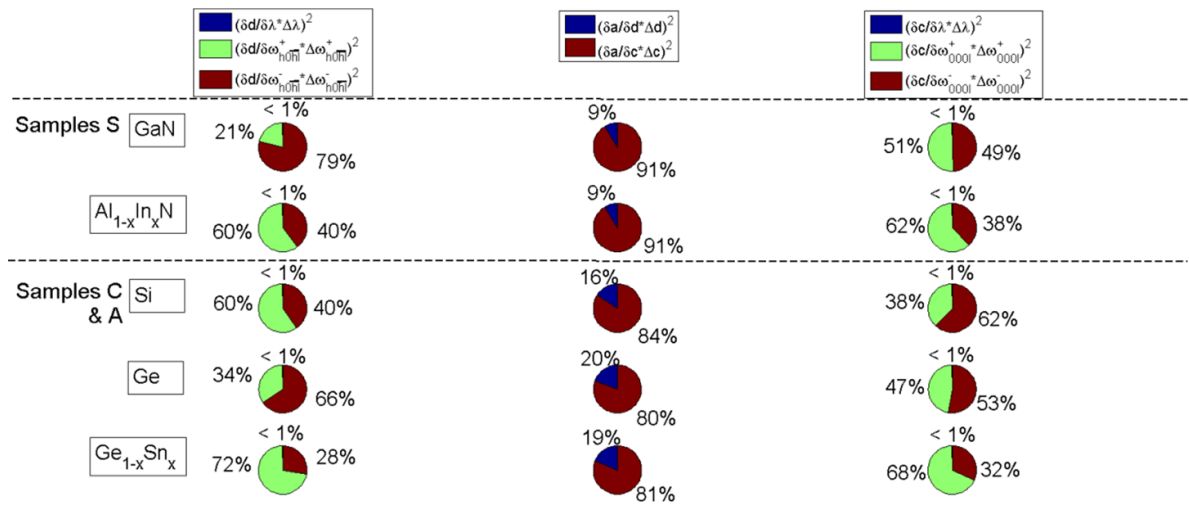
Figure 8. The relative weight of the major components in the inter-planar distance, *a*- and *c*-lattice parameter uncertainties, i.e. Δd, Δa and Δc calculated for samples S ($Al_{1-x}In_xN$ grown on GaN templates/substrate) and samples C ($Ge_{1-x}Sn_x$ grown on Ge templates and Si substrates).

Bravais lattices (wurtzite and cubic), Δd depends mainly on $\Delta\omega^+_{h0\bar{h}l}$ as its main source of uncertainty, while Δc is strongly dependent on $\Delta\omega^-_{000l}$.

4. Conclusions

The lattice parameters and chemical composition as well as respective uncertainties of four hexagonal MOCVD $Al_{1-x}In_xN$ and six cubic $Ge_{1-x}Sn_x$ layer compounds: three grown by MBE and three grown by CVD are determined and compared through reciprocal- and real space XRD techniques. The real-space measurements employ Bond's high accuracy method for determining the lattice parameters and are evaluated using the newly developed software-*LAPAs*, the acronym for 'Lattice parameters' while the reciprocal space maps are analysed by previously published RSM software. Refraction correction is included in the former and negligible impact was found on the overall lattice parameter's total uncertainties. Derived via reciprocal and real-space XRD techniques, the lattice parameters and chemical compositions of the $Al_{1-x}In_xN$ and $Ge_{1-x}Sn_x$ layers agree inside respective uncertainties. Specifically, with respect to the InN content, the four $Al_{1-x}In_xN$ compositions are found to be $0.147(4) \pm 0.005(3)$, $0.178(78) \pm 0.006(55)$, $0.205(45) \pm 0.006(55)$ and $0.220(4) \pm 0.006(59)$ if derived via the former method while 0.1469, 0.1773, 0.2012 and 0.2168 with uncertainties of 0.0002 if derived through the latter method. Both methodologies show close GaN and $Al_{1-x}In_xN$ in-plane lattice parameters in the four samples evidencing high levels of pseudomorphism. Furthermore, the relaxation degree determined via both reciprocal and real-space methods agree inside the respective uncertainties, i.e. $13 \pm 10\%$, $72 \pm 29\%$, $5 \pm 7\%$, and $5 \pm 6\%$ for the former and $2.7 \pm 0.1\%$, $68.2 \pm 0.1\%$, $1.7 \pm 0.1\%$ and $8.1 \pm 0.1\%$ calculated for the latter method. The relaxation degree of MBE and CVD $Ge_{1-x}Sn_x$ are also evaluated by reciprocal and real space-methods and

compared. As in the case of the nitrides, the relaxation was found to present high uncertainties if derived via the reciprocal space mapping motivated by the high uncertainties in the measured lattice parameters and consequently in the Sn contents. The employment of Bond's real-space method allows decreasing the uncertainties in the lattice parameters and the uncertainty in the Sn contents of the intervenient crystals in about ten times. In both crystallographic systems, the dominant uncertainty is found to be related to the Bragg's peak centre uncertainty while the smaller uncertainty is associated to the x-ray wavelength divergence ($\Delta\lambda/\lambda$).

Data availability statement

All data that support the findings of this study are included within the article (and any supplementary files).

Acknowledgments

ORCID iDs

S Magalhães ⬥ https://orcid.org/0000-0002-5858-549X
O Concepción ⬥ https://orcid.org/0000-0001-8197-7523
E Alves ⬥ https://orcid.org/0000-0003-0633-8937

J. Phys. D: Appl. Phys. **56** (2023) 245102

S Magalhães *et al*

References

[1] Magalhães S, Dias M, Nunes B, Oliveira F, Cerqueira M F and Alves E 2022 Confronting Vegard's rule in $Ge_{1-x}Sn_x$ epitalyers: from fundamentals to the effect of defects *J. Phys. D: Appl. Phys.* **52** 295301

[2] Fewster P F 2000 *X-Ray Scattering from Semiconductors* (London: Imperial College Press) (https://doi.org/10.1142/p137)

[3] Moram M A and Vickers M E 2009 X-ray diffraction of III-nitrides *Rep. Prog. Phys.* **72** 036502

[4] Metzger T *et al* 1998 Defect structure of epitaxial GaN films determined by transmission electron microscopy and triple axis-x-ray diffractometry *Phil. Mag.* A **77** 1013–25

[5] Magalhães S *et al* 2017 Validity of Vegard's rule for $Al_{1-x}In_xN$ (0.08 < x < 0.28) thin films grown on GaN templates *J. Phys. D: Appl. Phys.* **50** 205107

[6] Ayers J E 1994 The measurement of threading dislocation densities in semiconductor crystals by x-ray diffraction *J. Cryst. Growth* **135** 71–77

[7] Hino T, Tomiya S, Miyajima T, Yanashima K, Hashimoto S and Ikeda M 2000 Characterization of threading dislocations in GaN epitaxial layers *App. Phys. Lett.* **76** 23

[8] Hordon M J and Averbach B L 1961 X-ray measurement of dislocation density in deformed copper and aluminium single crystals *Acta Metall.* **9** 237–46

[9] Vegard L 1921 Die Konstitution der Mischkristalle und die Raumfüllung der Atome *Z. Phys.* **5** 17–26

[10] Hammond C 2015 *The Basics of Crystallography and Diffraction* 4th edn (Oxford: Oxford University Press)

[11] Sadd M H 2004 *Elasticity: Theory, Applications, and Numerics* 1st edn (New York: Academic)

[12] Darakchieva V, Xie M-Y, Tasnádi F, Abrikosov I A, Hultman L, Moneman B, Kamimura J and Kishino K 2008 Lattice parameters, deviations from Vegard's rule, and E_2 phonons in InAlN *Appl. Phys. Lett.* **93** 261908

[13] Lorenz K, Franco N, Alves E, Pereira S, Watson I M, Martin R W and O'Donnell K P 2008 Strain relaxation during AlInN growth on GaN *J. Cryst. Growth* **310** 4058

[14] Butté R *et al* 2007 *J. Phys. D: Appl. Phys.* **40** 6328–44

[15] Berger C, Dadgar A, Bläsing J, Franke A, Hempel T, Goldhahn R, Christen J and Krost A 2012 *Phys. Status Solidi* c **9** 1253–8

[16] Dadgar A, Schulze F, Bläsing J, Diez A, Krost A, Neuburger M, Kohn E, Daumiller I and Kunze M 2004 *Appl. Phys. Lett.* **85** 5400–2

[17] Gonschorek M, Carlin J-F, Feltin E, Py M A and Grandjean N 2006 *Appl. Phys. Lett.* **89** 062106

[18] Watson I M, Xiong C, Gu E, Dawson M D, Rizzi F, Bejtka K, Edwards P R and Martin R W 2008 *Proc. SPIE* **6993** 69930E

[19] Kasper E, Kittler M, Oehme M and Arguirov T 2013 Germanium tin: silicon photonics toward the mid-infrared *Photon. Res.* **1** 69

[20] Bauer M, Taraci J, Tolle J, Chizmeshya A V G, Zollner S, Smith D J, Menendez J, Changwu H and Kouvetakis J 2002 Ge-Sn semiconductors for band-gap and lattice engineering *Appl. Phys. Lett.* **81** 2992

[21] Gupta S, Köpe B M, Nishi Y and Saraswat, K C 2013 Achieving direct band gap in germanium through integration of Sn alloying and external strain *J. Appl. Phys.* **113** 073707

[22] Kouvetakis J, Menéndez J and Chizmeshya A V G 2006 Tin-based group IV semiconductors: new platforms for opto-and microelectronics in silicon *Ann. Rev. Mater. Res.* **36** 497

[23] Buca D *et al* 2022 Room temperature lasing in GeSn microdisks enabled by strain engineering *Adv. Opt. Mater.* **10** 22

[24] Tsukamoto T, Hirose N, Kasamatsu A, Mimura T, Matsui T and Suda Y 2015 Investigation of Sn surface segregation during GeSn epitaxial growth by auger electron spectroscopy and energy dispersive x-ray spectroscopy *Appl. Phys. Lett.* **106** 052103

[25] Kormoš L, Kratzer M, Kostecki K, Oehme M, Sikola T, Kasper E, Schulze J and Teichert C 2017 Surface analysis of epitaxially grown GeSn alloys with Sn contents between 15% and 18% *Surf. Interface Anal* **49** 297–302

[26] Lei W, Antoszewski J and Faraone L 2015 Progress, challenges, and opportunities for HgCdTe infrared materials and detectors *Appl. Phys. Rev.* **2** 041303

[27] Pan W W, Gu R J, Zhang Z K, Lei W, Umana-Membreno G A, Smith D J, Antoszewski J and Faraone L 2022 Defect engineering in MBE-grown CdTe buffer layers on GaAs (211)B substrates *J. Electron. Mater.* **51** 4869–83

[28] Pan W, Nath S K, Ma S, Re G Z, Fu Z L, Faraone L and Lei W 2022 Non-invasive and non-destructive characterization of MBE-grown CdZnTe/CdTe superlattice-based dislocation filtering layers *J. Appl. Phys.* **131** 205304

[29] Pan W W, Gu R J, Zhang Z K, Liu J L, Lei W and Faraone L 2020 Strained CdZnTe/CdTe superlattices as threading dislocation filters in lattice mismatched MBE growth of CdTe on GaSb *J. Electron. Mater.* **49** 6983–9

[30] Madni I, Umana-Membreno G A, Lei W, Gu R, Antoszewski J and Faraone L 2017 X-ray reciprocal space mapping of MBE grown HgCdTe on alternative substrates *Cryst. Res. Technol.* **52** 1700167

[31] Herres N, Kirste L, Obloh H, Köhler K, Wagner J and Koidl P 2002 *Mater. Sci. Eng.* **B91–2** 425–32

[32] Chen N F, Wang Y, He H and Lin L 1996 Effects of point defects on the lattice parameters of semiconductors *Phys. Rev.* B **54** 8516

[33] Hornstra J and Bartels W J 1978 Determination of the lattice constant of epitaxial layers of III-V compounds *J. Cryst. Growth* **44** 513–7

[34] Fewster P F and Andrew N L 1995 Absolute lattice-parameter measurement *J. Appl. Cryst.* **28** 451–8

[35] Krysko M, Domagala J Z, Czernecki R, Leszczynski M, Suski T, Sz G G, Grzegory T I, Bockowski M and Porowski S 2010 Tilt of InGaN layers on miscut GaN substrates *Rapid. Res. Lett.* **4** 142–4

[36] Perry W G, Zheleva T, Bremser M D, Davis R F, Shan W and Son J J 1997 Correlation of biaxial strains, bond exciton energies, and defect microstructures on GaN films grown on AlN/6H-SiC (0001) substrates *J. Electron. Mater.* **26** 224–31

[37] Luxium Solutions Headquarters (available at: www.crystals.saint-gobain.com/contact-us)

[38] Magalhães S, Barradas N P, Alves E, Watson I M and Lorenz K 2012 *Nucl. Instrum. Methods Phys. Res.* B **273** 105–8

[39] Watson I M, Liu C, Dawson M D, Edwards P R and Martin R W 2005 *Appl. Phys. Lett.* **87** 15190

[40] Kasper E, Werner J, Oehme M, Escoubas S, Burle N and Schulze J 2012 Growth of silicon based germanium tin alloys *Thin Solid Films* **520** 3195–200

[41] Werner J, Oehme M, Schirmer A, Kasper E and Schulze J 2012 Molecular beam epitaxy grown GeSn p-i-n photodetectors integrated on Si *Thin Solid Films* **520** 3361–4

[42] Wirths S *et al* 2015 Lasing in direct-bandgap GeSn alloy grown on Si *Nat. Photon.* **9** 88–92

[43] Blum P and Durif A 1956 Comparaison de deux méthodes de determination des constantes de réseau à l'aide d'un diffractomètre à rayons X, A *Acta Cryst.* **9** 829

[44] Cabaço J S, Nd D, Faye J P, Alves A E and Magalhães S 2021 Simulating the effect of Ar^+ energy implantation on the strain propagation in AlGaN *J. Phys. D: App. Phys.* **54** 245301

J. Phys. D: Appl. Phys. **56** (2023) 245102

S Magalhães *et al*

[45] Stachowicz M *et al* 2020 Study of structural and optical properties of MBE grown nonpolar (10-10) ZnO/ZnMgO photonic structures *Opt. Mater.* **100** 109709

[46] Mendes P, Lorenz K, Alves E, Schwaiger S, Scholz F and Magalhães S 2019 Measuring strain caused by ion implantation in GaN *Mater. Sci. Semicond. Process.* **98** 95–99

[47] Magalhães S *et al* 2014 Composition, structure and morphology of $Al_{1-x}In_xN$ thin films grown on $Al_{1-y}Ga_yN$ templates with different GaN contents *J. Phys. D: Appl. Phys.* **48** 015103

[48] Fialho M, Magalhães S, Chauvat M P, Ruterana P, Lorenz K and Alves E 2016 Impact of implantation geometry and fluence on structural properties of $Al_xGa_{1-x}N$ implanted with thulium *J. Appl. Phys.* **120** 165703

[49] Fialho M, Rodrigues J, Magalhães S, Correia M R, Monteiro T, Lorenz K and Alves E 2016 Effect of AlN content on the lattice site location of terbium ions in $Al_xGa_{1-x}N$ compounds *Semicond. Sci. Technol.* **31** 035026

[50] Fialho M, Magalhães S, Alves L, Marques C, Maalej R, Monteiro T, Lorenz K and Alves E 2016 AIN content influence on the properties of $Al_xGa_{1-x}N$ doped with Pr ions *Nucl. Instrum. Methods Phys. Res.* B **273** 149–52

[51] Yamaguchi M, Yagi T, Sota T, Deguchi T, Shimada K and Nakamura S 1999 Brillouin scattering study of bulk GaN *J. Appl. Phys.* **85** 8502

[52] Wright A F 1997 Elastic properties of zinc-blende and wurtzite AlN, GaN, and InN *J. Appl. Phys.* **82** 2833

[53] Tanaka M, Nakahata S, Sogabe K, Nakata H and Tabioka M 1997 Morphology and x-ray diffraction peak widths of aluminium nitride single crystals prepared by the sublimation method *Jpn. J. Appl. Phys.* **36** L1062

[54] Cerny P R and Krukowski R 2003 Rietveld diffraction from indium nitride in the 105–295 K range *Powder Diffr.* **18** 114

[55] Sheleg A U and Savastenko V A Izv. Akad. Nauk SSSR 1979 Determination of elastic constants of hexagonal crystals from measured values of dynamic atomic displacements *Neorg. Mater.* **15** 1598

[56] Nespolo M 2012 *Basic Elements of Crystallography* 1st edn, vol 68 (Abingdon: Pan Stanford) (https://doi.org/10.1107/S0108767312011968)

[57] Zhang L, Shao Y, Hao X, Wu Y, Qu X, Chen X and Xu X 2011 Comparison of the strain of GaN films grown on MOCVD-GaN/Al_2O_3 and MOCVD-GaN/SiC samples by HVPE growth *J. Cryst. Growth* **334** 62–66

[58] Kaganer V M and Sabelfeld K 2009 X-ray diffraction peaks from partially ordered misfit dislocations *Phys. Rev.* B **80** 184105

[59] Pietsch U, Holý V and Baumbach T 2004 *High-Resolution X-Ray Scattering, from Thin Films to Lateral Nanostructures* (*Advanced Texts in Physics*) (New York: Spring) (https://doi.org/10.1007/978-1-4757-4050-9)

[60] Schenk H P D, Nemoz M, Korytov M, Vennégués P, Dräger A D and Hangleiter A 2008 Indium incorporation dynamics into AlInN ternary alloys for laser structures lattice matched to GaN *Appl. Phys.* **93** 081116

[61] Vennégués P, Diaby B S, Chauveau H K, Bodiou L, Schenk H P D, Frayssinet E, Martin R W and Watson I M 2012 Nature and origin of V-defects present in metalorganic vapor phase epitaxy-grown $(In_xAl_{1-x})N$ layers as a function of the InN content, layer thickness and growth parameters *J. Cryst. Growth* **353** 108

[62] Sadler T C, Kappers M J and Oliver R A 2009 *J. Cryst. Growth* **311** 3380–5

[63] More J J 1978 *The Levenberg-Marquardt Algorithm: Implementation and Theory, Numerical Analysis* (Berlin: Springer) (available at: https://link.springer.com/content/pdf/10.1007/BFb0067700.pdf)

[64] Magalhães S, Cabaço J S, Araujo J P and Alves E 2021 Multiple reflection optimization package for x-ray diffraction *CrystEngComm* **23** 3308–18

[65] Magalhães S, Fialho M, Peres M, Lorenz K and Alves E 2016 Quantitative x-ray diffraction analysis of bimodal damage distributions in Tm implanted $Al_{0.15}Ga_{0.85}N$ *J. Phys. D: Appl. Phys.* **49** 135308

[66] Jozwik P, Magalhães S, Ratajczak R, Mieszczynski C, Sequeira M, Turos A, Andrzej B R, Heller R, Lorenz K and Alves E 2019 RBS/C, XRR, and XRD studies of damage buildup in Er-implanted ZnO *Phys. Status Solidi* b **256** 1800364

[67] Fialho M, Magalhães S, Rodrigues J, Chauvat M P, Ruterana P, Monteiro T, Lorenz K and Alves E 2018 Defect formation and optical activation of Tb implanted $Al_xGa_{1-x}N$ films using channeled implantation at different temperatures *Surf. Coat. Technol.* **355** 29–39